

Efficient Formulation of Ab Initio Quantum Embedding in Periodic Systems: Dynamical Mean-Field Theory

Tianyu Zhu, Zhi-Hao Cui, and Garnet Kin-Lic Chan*

*Division of Chemistry and Chemical Engineering, California Institute of Technology,
Pasadena, CA 91125, USA*

E-mail: gkc1000@gmail.com

Abstract

We present an efficient *ab initio* dynamical mean-field theory (DMFT) implementation for quantitative simulations in solids. Our DMFT scheme employs *ab initio* Hamiltonians defined for impurities comprising the full unit cell or a supercell of atoms and for realistic quantum chemical basis sets. We avoid double counting errors by using Hartree-Fock as the low-level theory. Intrinsic and projected atomic orbitals (IAO+PAO) are chosen as the local embedding basis, facilitating numerical bath truncation. Using an efficient integral transformation and coupled-cluster Green's function (CCGF) impurity solvers, we are able to handle embedded impurity problems with several hundred orbitals. We apply our *ab initio* DMFT approach to study a hexagonal boron nitride monolayer, crystalline silicon, and nickel oxide in the anti-ferromagnetic phase, with up to 104 and 78 impurity orbitals in spin-restricted and unrestricted cluster DMFT calculations and over 100 bath orbitals. We show that our scheme produces accurate spectral functions compared to both benchmark periodic coupled-cluster computations and experimental spectra.

1 Introduction

The accurate simulation of strongly correlated electronic materials requires many-body approximations beyond traditional mean-field and low-order perturbation theories. An important advance has been the development of dynamical mean-field theory (DMFT), both in its original single-site formalism,^{1,2} as well as in its cluster and multi-orbital extensions.³⁻⁶ In DMFT, the full interacting solid is mapped onto a local interacting impurity problem, where the impurity is taken to be a site or cell of local orbitals in the lattice. The impurity is described by its one-particle Green's function and is self-consistently embedded in an effective non-interacting environment via a hybridization self-energy. With an appropriate dimensional scaling, DMFT becomes exact in the limit of infinite dimensions⁷ as the only surviving contributions to the self-energy originate from local interactions. From a quantum chemical perspective, DMFT can also be viewed as a local correlation theory, because the non-local (inter-cell or inter-site) corrections to the mean-field self-energy are ignored.⁸

Combined with density functional theory (DFT),⁹ DMFT has successfully been used to describe many properties in strongly correlated d and f electron materials¹⁰⁻¹² including transition metal oxides, heavy fermion systems and high-temperature superconductors. The DFT+DMFT methodology starts with an *ab initio* DFT simulation of the material, which is then used to construct a material-specific low-energy effective Hamiltonian for a small number of localized, strongly interacting, d or f orbital bands. This proceeds via some form of “downfolding”,¹³⁻¹⁵ where the higher-energy degrees of freedom are approximately integrated out. Commonly, the effective Hamiltonian is taken to be of generalized Hubbard or Slater-Kanamori form^{16,17} where the one-electron matrix elements are the matrix elements of the mean-field Hamiltonian in a Wannier basis, and the interaction parameters (such as the Hubbard U parameter) are obtained empirically or via techniques such as constrained DFT^{18,19} or the constrained random phase approximation (cRPA).²⁰⁻²² After the effective Hamiltonian is derived, the corresponding DMFT impurity model is solved using a high-level impurity solver. This can be a numerically exact technique, such as continuous-time quantum

Monte Carlo (CT-QMC)^{23–25} or exact diagonalization (ED),^{26,27} or one of many different approximations, such as configuration interaction (CI),^{8,28} ansatz-based methods,^{29–31} or diagrammatic approximations.^{1,32,33} The strength of the DFT+DMFT scheme is that the itinerant electrons in the system can often be described well, and in a material specific way, by DFT, while the DFT hybridization and downfolded interactions yield material specific parameters in the small, strongly correlated impurity problem that can be treated accurately using the high-level many-body impurity solver.

Yet despite the successes of the DFT+DMFT approach, there are well-known drawbacks and challenges in the existing formulation and its numerical implementation. For example, although DFT does not accurately describe the strong correlation between localized d or f electrons, it nonetheless captures some portion of the interactions via the Hartree and exchange-correlation functionals. Such Coulomb interactions are also accounted for by DMFT within the downfolded impurity model, and the combination of the two leads to the prominent issue of double counting of correlations. This can be corrected for in a variety of ways,^{11,34–36} but much like in other DFT+wavefunction approaches,^{37–40} a consistently accurate and rigorously justifiable double counting correction is unknown. In addition, there can be numerical issues when downfolding to a low-energy effective Hamiltonian.^{41,42} For example, downfolding to a small number of bands is challenging because the effective particles are strongly renormalized, yielding strongly frequency dependent interactions, which is challenging for impurity solvers; downfolding to a large number of bands, on the other hand, requires extracting many parameters, which is difficult to do in a unique and well-conditioned way. In addition, even for a fixed size of low-energy subspace, various choices of Wannier orbitals can lead to substantially different interaction terms. Finally, the applicability of DMFT in *ab initio* simulations of realistic solids remains limited by the computational power of commonly used impurity solvers. At low temperatures, the CT-QMC solver is usually restricted to a single d -shell or f -shell impurity, due to the sign problem and the need for unstable analytic continuation for spectra,^{25,43} while ED solvers are restricted to

only 4 impurity sites, due to the exponential scaling with impurity size and the need for explicit bath orbitals.⁴⁴ Approximate methods, for example, based on CI, are naturally of lower cost,^{28,45,46} but even these in practice have only been used to treat a small number of interacting impurity orbitals.⁴⁷

To avoid some of the above issues of DFT+DMFT, alternative *ab initio* DMFT methodologies have been proposed. Zgid and Chan⁸ and Lin *et al.*⁴⁸ emphasized the Hartree-Fock (HF)+DMFT approach and further implemented DMFT without using any intermediate downfolded interactions, which might be termed a “quantum chemical” approach to DMFT. The theoretical reason to use HF+DMFT is that the contributions of the local interactions can be exactly subtracted, thus completely avoiding double counting, but the drawback is that non-local interactions (i.e. outside of the impurity) are described only at the HF level. To address this, more sophisticated diagrammatic methods for including long-range interactions have also been explored. The first was the GW+DMFT approach^{49–51} which starts from a beyond mean-field (e.g. GW) description of the solid, and subsequently self-consistently embeds the impurity self-energy and polarization propagator. More recently, Zgid and co-workers developed the self-energy embedding theory (SEET),^{52–54} which is similar to the above, but uses only the embedding of the self-energy. While these developments are promising, in practice, applications have remained more limited than those with DFT+DMFT and have sometimes retained problematic issues of that approach. For example, GW+DMFT has so far been applied within the downfolded Hamiltonian picture,^{51,55} rather than via a fully quantum chemical approach, while applications using HF+DMFT and SEET to infinite periodic systems, while retaining all interactions, have only appeared at the level of hydrogen cubes⁸ and 1D chains⁵⁴ in a minimal basis.

For quantitative predictions of experimentally relevant properties within the quantum chemical *ab initio* approach to DMFT, it is clear that one requires calculations beyond a few impurity orbitals and small basis sets. From our perspective, obstacles to such calculations have been technical rather than conceptual in nature. One significant obstacle has simply

been the complexity of implementing quantum chemistry, in other words, using realistic basis sets and computing all long-range matrix elements, in solids. However, recent years have seen new progress in periodic quantum chemistry infrastructure,^{56,57} and the situation is considerably advanced from the time of Ref.⁸ and Ref.⁴⁸ A second obstacle has been the lack of impurity solvers that can handle general (i.e. 4-index) Coulomb matrix elements for many orbitals. But similarly, recent implementations of DMRG-based Green’s function⁵⁸ and coupled-cluster Green’s function solvers^{33,59,60} for quantum chemical Hamiltonians, means that impurity problems with tens to hundreds of interacting orbitals are now practically accessible, depending on the strength of correlation.

In this work, we describe a quantum chemical framework for DMFT that takes advantage of these computational advances to enable quantitative calculations on non-trivial solids. Our implementation uses elements of the embedding implementation developed for density matrix embedding theory (DMET),^{61–63} described in a companion paper.⁶⁴ Based on this framework, we develop a DMFT algorithm that can treat impurities with a large number of orbitals in a realistic basis. For example, we take our impurity to be the full unit cell or even a supercell of atoms, in a basis of polarized valence double-zeta quality, yielding in our largest calculations impurities with over 100 orbitals. Several points should be highlighted. First, following the work of Zgid and Chan⁸ and Lin et al.,⁴⁸ our DMFT scheme starts from the HF approximation, and is thus free of double counting errors. While non-local interactions remain treated at the mean-field level, because our large impurities span multiple atoms, this significantly ameliorates the neglect of such non-local fluctuations. Second, in order to handle these large impurity problems, we rely on several techniques. First, we use a coupled-cluster (CC) impurity solver^{33,60} (at the coupled-cluster singles and doubles (CCSD) level) which allows us to treat more than 200 embedded (impurity plus bath) orbitals. In addition, we reuse the integral transformations described in the accompanying paper⁶⁴ and the efficient infrastructure of the Python-based Simulations of Chemistry Framework (PySCF)⁵⁶ to carry out the periodic mean-field and impurity Hamiltonian construction. Finally, we use

real-frequency bath construction and truncation techniques to systematically converge the DMFT hybridization and spectra.

This paper is organized as follows. In Sec. 2, we describe the DMFT formalism and the necessary ingredients in the computational framework, including the choice of local impurity basis, method of integral transformation and bath construction and truncation. We also recapitulate the use of CC impurity solvers in DMFT. The computational details are then shown in Sec. 3. In Sec. 4, we present DMFT results on several weakly and strongly correlated materials, including 2D hexagonal boron nitride, 3D bulk silicon, and nickel oxide in the antiferromagnetic (AFM) phase. We finally draw conclusions in Sec. 5.

2 Theory

2.1 DMFT formalism

In this section, we describe the DMFT formalism and the algorithm we use. Throughout this paper, we use the term DMFT to include both single-site DMFT and the more general cluster DMFT (CDMFT). Both DMFT and CDMFT have been extensively reviewed in the literature,^{6,10,12} so we only provide a description sufficient for the numerical considerations here. For example, we only describe bath-based DMFT while the bath-orbital-free DMFT formulations used with CT-QMC solvers are not discussed.

Consider the Hamiltonian of a periodic crystal in an orthogonal basis adapted to the translational symmetry of a unit cell \mathcal{C} (not necessarily primitive) with $N_{\mathcal{C}}$ sites,

$$\hat{H} = \sum_{pq \in \mathcal{C}} \sum_{\mathbf{k}} h_{pq}(\mathbf{k}) a_{p\mathbf{k}}^\dagger a_{q\mathbf{k}} + \frac{1}{2} \sum_{pqrs \in \mathcal{C}} \sum_{\mathbf{k}_p \mathbf{k}_q \mathbf{k}_r} V_{pqrs}(\mathbf{k}_p, \mathbf{k}_q, \mathbf{k}_r) a_{p\mathbf{k}_p}^\dagger a_{q\mathbf{k}_q}^\dagger a_{r\mathbf{k}_r} a_{s\mathbf{k}_p + \mathbf{k}_q - \mathbf{k}_r}, \quad (1)$$

where h_{pq} and V_{pqrs} are the one- and two-particle interaction matrix elements of the basis functions, indexed by labels in the unit cell \mathcal{C} , and momentum conservation is modulo lattice vectors. The non-interacting lattice Green's function is block-diagonal in \mathbf{k} space and can

be written as

$$\mathbf{g}(\mathbf{k}, \omega) = [(\omega + \mu)\mathbf{I} - \mathbf{h}(\mathbf{k})]^{-1}, \quad (2)$$

where μ is the chemical potential. The interacting lattice Green's function is related to the non-interacting Green's function via Dyson's equation:

$$\mathbf{G}(\mathbf{k}, \omega) = [\mathbf{g}^{-1}(\mathbf{k}, \omega) - \mathbf{\Sigma}(\mathbf{k}, \omega)]^{-1} = [(\omega + \mu)\mathbf{I} - \mathbf{h}(\mathbf{k}) - \mathbf{\Sigma}(\mathbf{k}, \omega)]^{-1}, \quad (3)$$

where the self-energy $\mathbf{\Sigma}(\mathbf{k}, \omega)$ accounts for the many-body correlation effects. The lattice Green's function in real space can then be obtained by a Fourier transform:

$$\mathbf{G}(\mathbf{R} = \mathbf{0}, \omega) = \frac{1}{N_{\mathbf{k}}} \sum_{\mathbf{k}} \mathbf{G}(\mathbf{k}, \omega), \quad (4)$$

and the local spectral function is defined as

$$\mathbf{A}(\mathbf{R} = \mathbf{0}, \omega) = -\frac{1}{\pi} \text{Im} \mathbf{G}(\mathbf{R} = \mathbf{0}, \omega + i0^+). \quad (5)$$

Directly computing the interacting lattice Green's function in the thermodynamic limit using an accurate many-body method is very expensive. Quantum embedding methods such as DMFT provide another route to this quantity. In DMFT, the periodic Hamiltonian in Eq. 1 is mapped onto an effective real-space impurity problem, where the unit cell \mathcal{C} (impurity) is embedded in a non-interacting environment. We will discuss the detailed form of the embedding Hamiltonian in the next section, and continue our focus on the general DMFT formalism here.

The key approximation in DMFT is to replace the \mathbf{k} -dependent lattice self-energy $\mathbf{\Sigma}(\mathbf{k}, \omega)$ with a local self-energy $\mathbf{\Sigma}_{\text{imp}}(\omega)$ defined for the $N_{\mathcal{C}}$ impurity sites:

$$\mathbf{\Sigma}(\mathbf{k}, \omega) = \mathbf{\Sigma}_{\text{imp}}(\omega). \quad (6)$$

Neglecting \mathbf{k} -dependence is equivalent to ignoring the off-diagonal self-energy between unit cells in real-space, which introduces a local correlation approximation. Given $\Sigma_{\text{imp}}(\omega)$, the lattice Green's function in Eq. 4 is approximated as

$$\mathbf{G}(\mathbf{R} = \mathbf{0}, \omega) = \frac{1}{N_{\mathbf{k}}} \sum_{\mathbf{k}} [(\omega + \mu)\mathbf{I} - \mathbf{h}(\mathbf{k}) - \Sigma_{\text{imp}}(\omega)]^{-1}. \quad (7)$$

To determine $\Sigma_{\text{imp}}(\omega)$ we solve a many-body problem for an embedded impurity, which is much simpler than the many-body problem for the the whole crystal. In the impurity problem, to describe the delocalization effects from the impurity-environment interaction, the hybridization self-energy is introduced:

$$\Delta(\omega) = (\omega + \mu)\mathbf{I} - \mathbf{h}_{\text{imp}} - \Sigma_{\text{imp}}(\omega) - \mathbf{G}^{-1}(\mathbf{R} = \mathbf{0}, \omega), \quad (8)$$

where \mathbf{h}_{imp} is the impurity one-particle Hamiltonian. When wavefunction-based impurity solvers (for example, CC in this work) are employed, the hybridization $\Delta(\omega)$ is mapped onto couplings between the impurity orbitals and a finite set of non-interacting bath sites. These interactions are included in the embedding Hamiltonian (see next section) which includes both the effects of local two-particle interactions, and delocalization into the environment. From the embedding Hamiltonian, the impurity Green's function $\mathbf{G}_{\text{imp}}(\omega)$ is computed by the many-body impurity solver, and the corresponding impurity self-energy $\Sigma_{\text{imp}}(\omega)$ is defined as

$$\Sigma_{\text{imp}}(\omega) = (\omega + \mu)\mathbf{I} - \mathbf{h}_{\text{imp}} - \Delta(\omega) - \mathbf{G}_{\text{imp}}^{-1}(\omega). \quad (9)$$

Since the impurity self-energy $\Sigma_{\text{imp}}(\omega)$ and hybridization $\Delta(\omega)$ are defined in terms of each other, the DMFT equations are solved self-consistently until the impurity Green's function $\mathbf{G}_{\text{imp}}(\omega)$ and the lattice Green's function $\mathbf{G}(\mathbf{R} = \mathbf{0}, \omega)$ agree:

$$\mathbf{G}_{\text{imp}}(\omega) = \mathbf{G}(\mathbf{R} = \mathbf{0}, \omega). \quad (10)$$

In practice, convergence of the self-consistency can be monitored also in terms of $\Sigma_{\text{imp}}(\omega)$ or the hybridization $\Delta(\omega)$. In this work, we assess convergence from the change of $\Delta(\omega)$ between DMFT iterations, and use the DIIS technique⁶⁵ to accelerate convergence.

2.2 Embedding Hamiltonian

We next describe how to construct the embedding Hamiltonian in DMFT. We take as our starting point the *ab initio* quantum embedding implementation for DMET discussed in Ref.⁶⁴ where several important computational choices and algorithms are discussed, including (1) defining the lattice and impurity basis starting from a mean-field calculation; (2) the choice of local orthogonal basis; (3) efficient integral transformation algorithms. We refer to Ref.⁶⁴ for additional details.

HF-based DMFT In Sec. 2.1, the DMFT formalism used the bare one-particle Hamiltonian in the definition of the non-interacting lattice Green’s function (Eq. 2). This is a reasonable choice for lattice models with purely local interactions, but in realistic solids, long-range Coulomb interactions play an important role. In this case, mean-field methods such as DFT and HF can be employed to provide the non-local self-energy between unit cells in DMFT.

In this work, we will only use Hartree-Fock non-local self-energies to avoid the double counting problems that arise when using DFT self-energies. The HF Green’s function is defined as

$$\mathbf{g}_{\text{HF}}(\mathbf{k}, \omega) = [(\omega + \mu)\mathbf{I} - \mathbf{F}(\mathbf{k})]^{-1}, \quad (11)$$

where $\mathbf{F}(\mathbf{k}) = \mathbf{h}(\mathbf{k}) + \Sigma_{\text{HF}}(\mathbf{k})$ is the lattice Fock matrix that includes the static HF self-energy $\Sigma_{\text{HF}}(\mathbf{k})$. The HF self-energy may be computed from a self-consistent HF solution of the crystal, or from a non-self-consistent density matrix and orbitals (such as DFT orbitals). Since the self-energy is diagrammatically defined in both cases, double-counting can be completely avoided.

The one-particle Hamiltonians in both the crystal and embedding problem are then replaced by the Fock matrix:

$$\mathbf{h}(\mathbf{k}) \rightarrow \mathbf{F}(\mathbf{k}), \quad \mathbf{h}_{\text{imp}} \rightarrow \mathbf{F}_{\text{imp}}. \quad (12)$$

For example, the lattice Green's function $\mathbf{G}(\mathbf{R} = \mathbf{0}, \omega)$ is now:

$$\mathbf{G}(\mathbf{R} = \mathbf{0}, \omega) = \frac{1}{N_{\mathbf{k}}} \sum_{\mathbf{k}} [(\omega + \mu)\mathbf{I} - \mathbf{F}(\mathbf{k}) - \Sigma_{\text{imp}}(\omega)]^{-1}. \quad (13)$$

Accordingly, the definition of the impurity self-energy $\Sigma_{\text{imp}}(\omega)$ also changes:

$$\Sigma_{\text{imp}}(\omega) = (\omega + \mu)\mathbf{I} - \mathbf{F}_{\text{imp}} - \Delta(\omega) - \mathbf{G}_{\text{imp}}^{-1}(\omega). \quad (14)$$

In this work, where we use CC as the impurity solver (see below), this implies that $\Sigma_{\text{imp}}(\omega)$ is taken as the difference between the CC self-energy and HF self-energy of the impurity:

$$\Sigma_{\text{imp}}(\omega) = \Sigma_{\text{imp}}^{\text{CC}}(\omega) - \Sigma_{\text{imp}}^{\text{HF}}. \quad (15)$$

One subtlety to consider is the density matrix to use when computing $\Sigma_{\text{imp}}^{\text{HF}}$. In a charge self-consistent DMFT calculation, one updates the lattice Fock matrix and impurity Hartree-Fock self-energy using correlated lattice and impurity density matrices. In this work, we use the initial mean-field impurity density matrix from lattice HF or DFT calculations to build $\Sigma_{\text{imp}}^{\text{HF}}$ and keep $\Sigma_{\text{imp}}^{\text{HF}}$ fixed during the DMFT iterations. We leave a charge self-consistent implementation to future work.

Local orthogonal orbital basis Until now, we have assumed an orthogonal basis in the formalism. However, in our mean-field calculations we use crystal Gaussian atomic orbitals (AO), which are not orthogonal. While it is possible to formulate DMFT with Green's functions and matrix elements in a non-orthogonal basis, the hybridization $\Delta(\omega)$ acquires

a non-trivial high frequency tail that can be hard to represent in a bath formulation.^{4,8} Therefore, it is desirable to work with an orthogonal atom-centered (crystal) local orbital (LO) basis.

As discussed in Ref.⁶⁴ for *ab initio* DMET, we will employ intrinsic (crystal) atomic orbitals and projected (crystal) atomic orbitals (IAO+PAO)^{63,66} as the local orthogonal basis. IAOs are a set of valence atomic-like orbitals that exactly span the occupied space of the mean-field calculations, and whose construction only requires projecting the HF/DFT orbitals onto pre-defined valence (minimal) AOs. PAOs, on the other hand, provide the remaining high-energy virtual atomic-like orbitals that are orthogonal to the IAO space. The main advantage of the IAO+PAO scheme is that no numerical optimization is needed to construct the LOs and the mean-field valence and virtual spaces are explicitly separated.

From the IAO+PAO projections, a transformation matrix from crystal AOs to crystal LOs at each \mathbf{k} point $C^{\mathbf{k},\text{AO},\text{LO}}$ can be obtained. The real-space one-particle Hamiltonian, Fock matrix and density matrix in the impurity LO basis are computed as:

$$\mathbf{h}_{\text{imp}} = \frac{1}{N_{\mathbf{k}}} \sum_{\mathbf{k}} \mathbf{h}^{\text{LO}}(\mathbf{k}) = \frac{1}{N_{\mathbf{k}}} \sum_{\mathbf{k}} C^{\mathbf{k},\text{AO},\text{LO}\dagger} \mathbf{h}^{\text{AO}}(\mathbf{k}) C^{\mathbf{k},\text{AO},\text{LO}}, \quad (16)$$

$$\mathbf{F}_{\text{imp}} = \frac{1}{N_{\mathbf{k}}} \sum_{\mathbf{k}} \mathbf{F}^{\text{LO}}(\mathbf{k}) = \frac{1}{N_{\mathbf{k}}} \sum_{\mathbf{k}} C^{\mathbf{k},\text{AO},\text{LO}\dagger} \mathbf{F}^{\text{AO}}(\mathbf{k}) C^{\mathbf{k},\text{AO},\text{LO}}, \quad (17)$$

$$\gamma_{\text{imp}} = \frac{1}{N_{\mathbf{k}}} \sum_{\mathbf{k}} \gamma^{\text{LO}}(\mathbf{k}) = \frac{1}{N_{\mathbf{k}}} \sum_{\mathbf{k}} C^{\mathbf{k},\text{AO},\text{LO}\dagger} \mathbf{S}(\mathbf{k}) \gamma^{\text{AO}}(\mathbf{k}) \mathbf{S}(\mathbf{k}) C^{\mathbf{k},\text{AO},\text{LO}}, \quad (18)$$

where $\gamma^{\text{AO}}(\mathbf{k})$ and $\mathbf{S}(\mathbf{k})$ are the one-particle density matrix and overlap matrix in \mathbf{k} space.

The impurity Hamiltonian can then be formulated as:

$$\hat{H}_{\text{imp}} = \sum_{ij \in \text{imp}} \tilde{F}_{ij} a_i^\dagger a_j + \frac{1}{2} \sum_{ijkl \in \text{imp}} (ij|kl) a_i^\dagger a_k^\dagger a_l a_j, \quad (19)$$

where i, j, k, l stand for impurity local orbitals and $(ij|kl)$ denotes a two-electron repulsion integral (ERI). To avoid double counting in DMFT, the Hartree-Fock contribution to the

impurity self-energy needs to be removed from the one-particle impurity Hamiltonian:

$$\tilde{F}_{ij} = (F_{\text{imp}})_{ij} - \sum_{kl \in \text{imp}} (\gamma_{\text{imp}})_{kl} [(ij|lk) - \frac{1}{2}(ik|lj)]. \quad (20)$$

This subtraction eliminates double counting in HF-based DMFT.

ERI transformation The most expensive step in forming the impurity Hamiltonian is to construct the impurity ERIs $(ij|kl)$. In our implementation, we start from the \mathbf{k} -space Gaussian density fitting (GDF)^{67,68} AO integrals $(L\mathbf{k}_L|p\mathbf{k}_pq\mathbf{k}_q)$, where L is a crystal Gaussian auxiliary basis. Note that \mathbf{k}_L , \mathbf{k}_p and \mathbf{k}_q satisfy momentum conservation modulo lattice vectors: $\mathbf{k}_L = \mathbf{k}_p - \mathbf{k}_q$. The detailed ERI transformation algorithm is presented in Algorithm 1. This algorithm scales as $\mathcal{O}(n_{\mathbf{k}}^2 n_L n_{\text{AO}}^3)$ for the \mathbf{k} -AO to \mathbf{k} -LO transformation step and $\mathcal{O}(n_{\mathbf{k}} n_L n_{\text{AO}}^4)$ for the ERI contraction step. This should be compared to the steep $\mathcal{O}(n_{\mathbf{k}}^3 n_{\text{AO}}^5)$ scaling of the transformation without density fitting techniques. We note that this algorithm is the same as would be used for the ERI transformation in the non-interacting bath formalism of DMET.

Algorithm 1 Pseudocode for the impurity ERI transformation in DMFT using GDF.

- 1: **for** all \mathbf{k}_L **do**
 - 2: **for** $(\mathbf{k}_p, \mathbf{k}_q)$ that conserves momentum **do**
 - 3: Transform $(L|p\mathbf{k}_pq\mathbf{k}_q)$ to $(L|i\mathbf{k}_pj\mathbf{k}_q)$ by $C^{\mathbf{k},\text{AO},\text{LO}}$ ▷ \mathbf{k} -AO to \mathbf{k} -LO
 - 4: $(L|\mathbf{0}i\mathbf{0}j) += \frac{1}{N_{\mathbf{k}}}(L|i\mathbf{k}_pj\mathbf{k}_q)$ ▷ FT to the reference cell $\mathbf{R} = \mathbf{0}$
 - 5: **end for**
 - 6: $(ij|kl) += \frac{1}{N_{\mathbf{k}}} \sum_L (\mathbf{0}i\mathbf{0}j|L)(L|\mathbf{0}k\mathbf{0}l)$ ▷ ERI contraction
 - 7: **end for**
-

Bath truncation In bath-based DMFT, the hybridization $\Delta(\omega)$ is represented by a finite set of discrete bath sites and couplings. In this work, we choose to approximate $\Delta(\omega)$ along the real frequency axis^{29,46,69,70} so that dynamical quantities (e.g. spectral functions) can be computed more accurately than when fitting along the imaginary frequency axis.^{44,71,72} We

consider $\Delta(\omega)$ as the Hilbert transform⁷³

$$\Delta(\omega) = \int \frac{\mathbf{J}(\epsilon)}{\omega - \epsilon} d\epsilon \quad (21)$$

with the spectral density

$$\mathbf{J}(\epsilon) = -\frac{1}{\pi} \mathbf{Im} \Delta(\epsilon + i\eta), \quad (22)$$

where η is a broadening parameter. The Hilbert transform integral can be approximated by a numerical quadrature (Gauss-Legendre in this work) along the real axis

$$\Delta(\omega) = \sum_{n=1}^{N_\omega} w_n \frac{\mathbf{J}(\epsilon_n)}{\omega - \epsilon_n}, \quad (23)$$

where w_n and ϵ_n are the weights and positions of the N_ω quadrature grid points. To derive the couplings between the impurity and bath sites, we diagonalize the spectral density

$$\mathbf{J}(\epsilon_n) = \mathbf{U}^{(n)} \lambda^{(n)} \mathbf{U}^{(n)\dagger}. \quad (24)$$

Eq. 23 then becomes:

$$\Delta_{ij}(\omega) = \sum_{n=1}^{N_\omega} \sum_{k=1}^{N_c} \frac{V_{ik}^{(n)} V_{jk}^{(n)}}{\omega - \epsilon_n}, \quad (25)$$

with

$$V_{ik}^{(n)} = w_n^{\frac{1}{2}} U_{ik}^{(n)} (\lambda_{kk}^{(n)})^{\frac{1}{2}}. \quad (26)$$

Thus, $V_{ik}^{(n)}$ and ϵ_n can be interpreted as the impurity-bath couplings and energy levels of bath orbitals. With this bath discretization, we can finally define the full embedding Hamiltonian

$$\hat{H}_{\text{emb}} = \hat{H}_{\text{imp}} + \sum_{n=1}^{N_\omega} \sum_{k=1}^{N_c} \left(\sum_i V_{ik}^{(n)} (a_i^\dagger a_{nk} + a_{nk}^\dagger a_i) + \epsilon_n a_{nk}^\dagger a_{nk} \right). \quad (27)$$

It is known that bath discretization introduces discretization errors into DMFT, thus many bath orbitals per impurity site are required to minimize this error. In our case, the

number of bath orbitals is formally $N_b = N_\omega N_{\mathcal{C}}$, which can easily be as many as a few hundred, as $N_{\mathcal{C}}$ includes all orbitals in the unit cell. To reduce the bath size and thus computational cost, we employ several strategies to truncate the bath degrees of freedom, while minimizing the error introduced. First, we only couple bath orbitals to the IAOs (valence orbitals). Note that PAOs (non-valence virtuals) are still included in the embedding problem and interact with the IAOs. With this choice, the number of bath orbitals is reduced to $N_b = N_\omega N_{\text{IAO}}$. Second, we remove the bath orbitals which are very weakly coupled to the impurity. As seen in Eq. 26, the scale of the bath coupling is set by the eigenvalues $\lambda_{kk}^{(n)}$. By dropping the bath orbitals with eigenvalues below a threshold, we can further decrease the bath dimension as necessary.

We have now described all the ingredients needed to perform *ab initio* DMFT calculations in a practical and efficient manner in realistic solids. For clarity, we summarize the detailed steps in Algorithm 2. Note that the chemical potential μ is adjusted to ensure the electron count of the impurity is correct (in these calculations, since multiples of the full unit cell are used as the impurity and there is no doping, the impurity electron count is an integer).

Algorithm 2 Pseudocode for *ab initio* DMFT in realistic solids.

- 1: IAO+PAO construction
 - 2: Integral transformation: Eqs. 16-18 and Algorithm 1
 - 3: **Input:** N_e (electron number in \mathcal{C}), N_ω and quadrature range
 - 4: **while** $|\text{Tr}\gamma_{\text{imp}}^{\text{CC}} - N_e| > \delta_e$ **do**
 - 5: Choose chemical potential μ
 - 6: Initial guess of impurity self-energy $\Sigma_{\text{imp}}(\omega)$
 - 7: Initialize hybridization $\Delta(\omega)$ via Eq. 8 \triangleright HF hybridization if $\Sigma_{\text{imp}}(\omega) = \mathbf{0}$
 - 8: **while** $\|\Delta_{i+1}(\omega) - \Delta_i(\omega)\| > \theta$ **do**
 - 9: Discretize $\Delta(\omega)$ via Eq. 25
 - 10: Form \hat{H}_{emb} via Eq. 27
 - 11: Solve embedding problem with HF at fixed μ \triangleright Electron number can change
 - 12: Compute $\mathbf{G}_{\text{imp}}(\omega)$ using CCSD-GF solver
 - 13: Calculate $\Sigma_{\text{imp}}(\omega)$ via Eq. 14
 - 14: Calculate $\Delta(\omega)$ via Eq. 8 and update using DIIS
 - 15: **end while**
 - 16: **end while**
 - 17: Compute $\mathbf{G}(\mathbf{R} = \mathbf{0}, \omega)$ over desired frequencies via Eq. 13
-

2.3 Coupled-cluster impurity solvers

In this work, we will use a coupled-cluster (CC) impurity solver to compute $\mathbf{G}_{\text{imp}}(\omega)$ from the embedding Hamiltonian in Eq. 27. We recently studied the coupled-cluster Green’s function (CCGF) approximation as an impurity solver in DMFT³³ (see also Ref.⁶⁰) and showed that it performed well for small impurity clusters in Hubbard models. Here, we further explore its capabilities in the *ab initio* setting.

A detailed presentation of the CCGF formalism can be found in Refs.^{33,59,74–77} Here, we will only comment on a few points related to DMFT. First, we use the coupled-cluster singles and doubles Green’s function approximation (CCSD-GF) as the impurity solver here. The cost of ground-state CCSD scales as $\mathcal{O}(N_{\text{emb}}^6)$ and CCSD-GF scales as $\mathcal{O}(N_{\omega}N_{\mathcal{C}}N_{\text{emb}}^5)$, where N_{emb} is the total number of orbitals (sites) in the embedding problem and $N_{\mathcal{C}}$ is the number of impurity orbitals. In practice, the CCSD-GF calculation can be parallelized over N_{ω} and $N_{\mathcal{C}}$. This low cost compared to ED allows us to treat around 200 embedding orbitals in DMFT. Second, the CCSD-GF is computed directly on the real frequency axis with a broadening factor η . We find that in *ab initio* calculations, when η is small (< 0.5 eV), causality issues may exist where the imaginary part of the CCSD self-energy is not always negative (see Fig. S2 for an example). We refer readers to Ref.³³ for a practical solution, where one computes the impurity plus bath self-energy and then uses the impurity block of the self-energy matrix, instead of directly computing the impurity self-energy matrix. This solution increases the CCSD-GF cost scaling slightly to $\mathcal{O}(N_{\omega}N_{\text{emb}}N_{\text{emb}}^5)$. We use this more expensive technique in the final calculation of spectra after DMFT convergence.

3 Computational Details

We applied the above DMFT scheme to study three realistic solids: weakly correlated 2D hexagonal boron nitride (h-BN) and crystalline silicon (Si), and a prototypical “strongly correlated” problem, nickel oxide (NiO) in the AFM-II phase. The experimental lattice

constants were used for all calculations: 2.50Å for h-BN monolayer,⁷⁸ 5.417Å for Si⁷⁹ and 4.17Å for NiO.⁸⁰ For h-BN, we used a vacuum spacing of 20Å along the z axis to avoid image interactions between neighboring sheets. In h-BN and Si we used (super)cells of the primitive cell as the impurity. In NiO, we used a supercell with two Ni and two O atoms along the [111] direction to allow for AFM spin symmetry breaking within the cell.

All mean-field calculations were performed and all integrals were generated using the PYSCF quantum chemistry package.⁵⁶ Norm-conserving GTH-PADE pseudopotentials^{81,82} were employed to replace the core electrons. The GTH-DZVP basis set was used for h-BN and Si, while the GTH-DZVP-MOLOPT-SR basis set⁸³ was used for NiO. This corresponds to 26, 26 and 78 AOs in the impurity unit cells of h-BN, Si and NiO, and 104 AOs in our largest impurity supercell of Si. The minimal basis sets GTH-SZV (h-BN and Si) and GTH-SZV-MOLOPT-SR (NiO) were used as the pre-defined AOs to construct the IAOs, leading to 8, 8 and 28 valence orbitals in each unit cell respectively. Even-tempered auxiliary Gaussian basis sets were used to compute the GDF integrals. Uniform $6 \times 6 \times 1$ (h-BN), $4 \times 4 \times 4$ (Si) and $4 \times 4 \times 4$ (NiO) \mathbf{k} -point meshes were adopted for the mean-field and DMFT calculations. All meshes were Γ -centered.

Unless otherwise specified, we used HF as the initial lattice mean-field in the DMFT embedding. The CCSD-GF method was implemented based on the CCSD and EOM-CCSD routines from the PYSCF package, and the DMFT algorithm was implemented in the POTATO module. A spin-restricted CCSD-GF (RCCSD-GF) solver was used for h-BN and Si, while a spin-unrestricted CCSD-GF (UCCSD-GF) solver within the spin-unrestricted DMFT formalism was employed for NiO. A simplified and flexible variant of the GCROT method (GCROT(m, k))⁸⁴ was used to solve the CCSD-GF linear response equations. Gauss-Legendre quadrature was used on frequency intervals of $[-1.0 + \mu, 1.0 + \mu]$ a.u. (h-BN), $[-0.6 + \mu, 1.0 + \mu]$ a.u. (Si) and $[-0.5 + \mu, 0.5 + \mu]$ a.u. (NiO) when discretizing the hybridization. We used a broadening factor of $\eta = 0.1$ a.u. during the DMFT self-consistent cycles and switched to a smaller η (depending on the required resolution) in the

final production runs to compute $\mathbf{G}(\mathbf{R} = \mathbf{0}, \omega)$. The DMFT self-consistency was converged to $\|\Delta_{i+1}(\omega) - \Delta_i(\omega)\| < \theta = 10^{-4}$ a.u. between two DMFT iterations.

4 Results and Discussion

4.1 2D h-BN

We first investigate the performance of our *ab initio* DMFT scheme for the 2D h-BN monolayer. We chose the impurity to be an h-BN unit cell, including the $2s2p3s3p3d$ orbitals for both boron and nitrogen atoms (26 impurity orbitals in total). The corresponding IAOs are projected $2s2p$ orbitals, giving 8 IAOs coupled to the bath. To study the convergence of DMFT with respect to the number of bath orbitals, we used a series of Gauss-Legendre quadratures to discretize the hybridization: $N_\omega = 4, 8, 12, 16$. This led to a total number of $N_b = 32, 64, 96, 128$ bath orbitals.

Table 1: Direct and indirect band gaps (in eV) of 2D h-BN.

Method	$\mathbf{K} \rightarrow \mathbf{K}$	$\mathbf{K} \rightarrow \mathbf{\Gamma}$	$\mathbf{\Gamma} \rightarrow \mathbf{\Gamma}$
HF	11.31	10.70	13.14
PBE	4.61	5.90	7.37
DMFT(i26,b32)	5.69	6.85	10.10
DMFT(i26,b64)	7.23	7.76	9.63
DMFT(i26,b96)	7.61	8.00	9.75
DMFT(i26,b128)	7.73	8.08	9.76
EOM-CCSD ($3 \times 3 \times 1$)	9.50	9.36	11.44
EOM-CCSD ($6 \times 6 \times 1$)	7.48	7.78	9.78

The computed direct and indirect band gaps at special \mathbf{k} points are presented in Table 1. In this paper, we use the notation “DMFT(iX,bY)” to mean that there are X impurity orbitals and Y bath orbitals to be treated by the CCSD-GF impurity solver. The DMFT band gaps are calculated from the valence and conduction peaks of \mathbf{k} -resolved density of states (DOS). We compare our DMFT results to HF, DFT/PBE⁸⁵ and EOM-CCSD^{86,87} gaps computed using PYSCF, all with $6 \times 6 \times 1$ \mathbf{k} -point meshes. EOM-CCSD with $3 \times 3 \times 1$

\mathbf{k} -point sampling is also included for comparison. As shown in Table 1, $6 \times 6 \times 1$ EOM-CCSD with the GTH-DZVP basis predicts that 2D h-BN is a direct band-gap semiconductor, with a gap of 7.48 eV at the \mathbf{K} point. The indirect band gap from \mathbf{K} to $\mathbf{\Gamma}$ has a slightly larger value of 7.78 eV. These values are taken as the reference values. Compared to $6 \times 6 \times 1$ EOM-CCSD, HF overestimates the $\mathbf{K} \rightarrow \mathbf{K}$ gap by 3.8 eV, while PBE underestimates it by 2.9 eV. EOM-CCSD with a smaller $3 \times 3 \times 1$ \mathbf{k} mesh also overestimates the band gaps by 1.6-2.0 eV, suggesting the importance of large \mathbf{k} -point meshes to approach the thermodynamic limit.

Even with a small number (32) of bath orbitals, our DMFT(i26,b32) result shows significant improvement over mean-field methods, although the $\mathbf{K} \rightarrow \mathbf{K}$ gap is still underestimated by 1.8 eV. As we increase the number of bath orbitals N_b to 64, DMFT produces a better description of all three band gaps and the errors are all within 0.3 eV, indicating the necessity of using a sufficient number of bath orbitals to reduce the bath discretization error. Even with a $1 \times 1 \times 1$ unit cell as the impurity, the DMFT(i26,b64) result is superior to the EOM-CCSD ($3 \times 3 \times 1$) result due to the larger amount of \mathbf{k} -point sampling. By further increasing N_b to 128, we also demonstrate that the DMFT band gaps are converged to around 0.1 eV at $N_b = 96$. Thus, we believe our DMFT results for 2D h-BN to be well converged with respect to the bath size. In addition, to investigate the effect of not coupling bath orbitals to the PAO space, we further compare the IAO-only hybridization against the full IAO+PAO hybridization near the Fermi surface from the converged DMFT(i26,b96) calculation, as shown in Fig. S1 (Supporting Information). There we observe that the IAO-only hybridization captures the low-energy physics very well compared to the IAO+PAO hybridization, indicating that the error introduced by this approximation is very small. The DMFT(i26,b96) calculation takes 1.5 hours to converge on 2 nodes with 28 CPU cores per node. Further obtaining the Green's function and DOS at each frequency point takes about 4.5 minutes. This should be compared to the computational cost of a full EOM-CCSD calculation with the $6 \times 6 \times 1$ \mathbf{k} -point mesh, which takes about 40 hours to obtain 4 IP and EA roots at all

\mathbf{k} points.

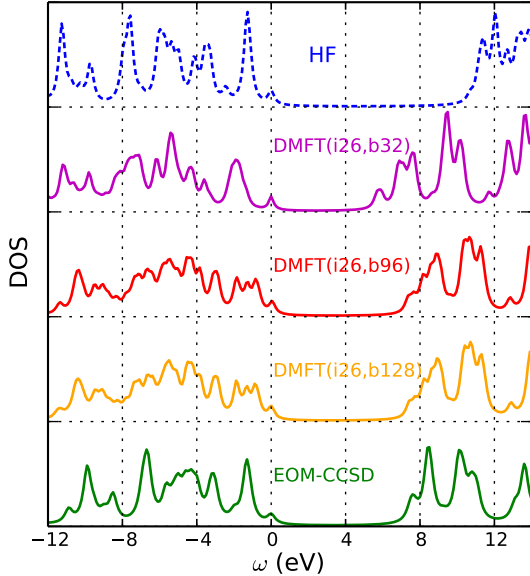


Figure 1: Local density of states of 2D h-BN monolayer. DMFT spectral functions are computed with a broadening factor $\eta = 0.2$ eV. EOM-CCSD ($6 \times 6 \times 1$) DOS is generated using a Lorentzian broadening.

We next show the local density of states (DOS) in Fig. 1, where the DOS is computed from the spectral function: $\rho(\mathbf{R} = \mathbf{0}, \omega) = \text{Tr} \mathbf{A}(\mathbf{R} = \mathbf{0}, \omega)$. Here we compare DMFT with HF and $6 \times 6 \times 1$ EOM-CCSD. Since we employ only a single \mathbf{k} -point mesh to minimize cost, we only obtain a finite set of excitation energies from EOM-CCSD. Consequently, we have applied a Lorentzian broadening to the IP- and EA-EOM-CCSD roots to generate the corresponding DOS spectrum, as an approximation to the true CCSD-GF DOS in the TDL. As can be seen in Fig. 1, DMFT again significantly improves over HF. In addition to the much better band gaps, the DMFT DOS also has a better structure than the HF DOS. In particular, the DMFT conduction bands are almost identical to the EOM-CCSD ones, even for the high-energy bands. This is a result of including the high-energy virtual orbitals (PAOs) into the impurity problem. Comparing the DMFT(i26,b96) and DMFT(i26,b128) DOS plots, we find that the DMFT spectral functions are already well converged at $N_b = 96$.

On the other hand, the agreement between the DMFT DOS of the valence bands and that

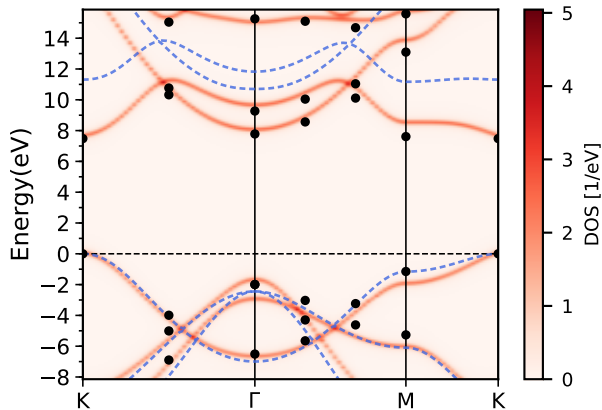


Figure 2: Band structure of 2D h-BN from DMFT(i26,b96) calculation with a broadening factor $\eta = 0.1$ eV (heat map). The blue dashed lines represent the HF band structure and the black circles are EOM-CCSD ($6 \times 6 \times 1$) charged excitation energies.

of EOM-CCSD is less perfect. Compared to EOM-CCSD, several valence peaks are broader in DMFT, such as the valence peak near the Fermi surface. To understand this behavior, we plotted the DMFT band structure of h-BN using the $N_b = 96$ data, as presented in Fig. 2. Compared to HF, we find that the point group symmetry at certain \mathbf{k} points is broken in the DMFT band structure plot. For example, at the Γ point, there is a degeneracy in the highest valence band observed in both HF and EOM-CCSD, but this degeneracy is slightly broken in DMFT. This explains the broader DMFT valence bands in Fig. 1. We believe such behavior is due to a mismatch between the diagonal and off-diagonal parts of self-energy in DMFT: the diagonal part is computed from the impurity CCSD-GF, while the off-diagonal part is from the lattice \mathbf{k} -point HF self-energy. Aside from the slight symmetry breaking, the DMFT band structure is in good agreement with the EOM-CCSD result.

Overall, however, the data demonstrates that our DMFT scheme works well in 2D h-BN. The DMFT procedure produces accurate band gaps and is also capable of modeling bands far away from the Fermi surface, even with a small number of bath orbitals ($N_b = 64$).

4.2 Bulk Si

We next apply our DMFT implementation to the silicon crystal (Si). Silicon is a small band-gap semiconductor with delocalized valence electrons. Such a system presents a challenge to quantum embedding methods, including DMFT, as these methods all start from a local correlation approximation. Here, we assess the effect of impurity size on the description of spectral functions of bulk Si. Two different impurity sizes were considered: a $1 \times 1 \times 1$ unit cell and a $2 \times 2 \times 1$ supercell. The $2 \times 2 \times 1$ cell is the largest impurity size that can currently be handled using our CCSD-GF solver. In the $1 \times 1 \times 1$ unit cell, there are 26 impurity orbitals, 8 of which are IAOs. Two Gauss-Legendre quadratures of $N_\omega = 4, 20$ ($N_b = 32, 160$) were used to show the effect of bath size on spectral functions. In the $2 \times 2 \times 1$ supercell impurity, there are 104 impurity orbitals. There we used a quadrature of $N_\omega = 4$ ($N_b = 128$). A $2 \times 2 \times 4$ \mathbf{k} -mesh was employed for the larger impurity to generate a DMFT lattice $4 \times 4 \times 4$ \mathbf{k} -mesh. We note that DMFT(i104,b128) should be directly compared to DMFT(i26,b32) to demonstrate the effect of impurity size, as these calculations share the same bath quadrature ($N_\omega = 4$) and similar bath discretization error.

The computed local DOS of bulk Si are presented in Fig. 3. HF and EOM-CCSD results are included for comparison. A full $4 \times 4 \times 4$ \mathbf{k} -point EOM-CCSD calculation for multiple IP/EA roots is very expensive, so we instead performed a $3 \times 3 \times 3$ \mathbf{k} -mesh calculation. All \mathbf{k} points in the $4 \times 4 \times 4$ \mathbf{k} -mesh were sampled by shifting the $3 \times 3 \times 3$ \mathbf{k} -mesh center. The final reference DOS was then generated by applying a Lorentzian broadening. We also conducted a full $4 \times 4 \times 4$ \mathbf{k} -mesh EOM-CCSD calculation to estimate the reference indirect $\Gamma \rightarrow \mathbf{X}$ band gap value, which we found to be 1.27 eV, as noted in Fig. 3.

DMFT(i26,b32) produces a better $\Gamma \rightarrow \mathbf{X}$ gap of 1.90 eV than HF, which overestimates the gap by 2.8 eV. Using a larger bath size of $N_b = 160$ further improves the DMFT gap to be 1.74 eV. However, the error of DMFT(i26,b160) is still around 0.5 eV, which is worse than the observed error of DMFT in 2D h-BN. In addition, the shape of the spectrum for DMFT(i26,b160) is not very accurate. These results support the observation that bulk Si is

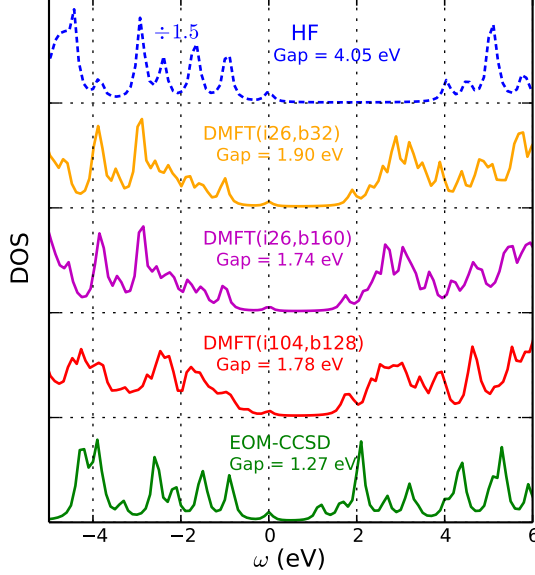


Figure 3: Local density of states of bulk Si. DMFT spectral functions are computed with a broadening factor $\eta = 0.1$ eV. The EOM-CCSD DOS is generated using $3 \times 3 \times 3$ \mathbf{k} -point sampling and a Lorentzian broadening. The gap values correspond to the indirect band gap of $\Gamma \rightarrow \mathbf{X}$, and the EOM-CCSD gap is from a $4 \times 4 \times 4$ \mathbf{k} -mesh calculation.

indeed a more difficult system for DMFT due to the stronger effects of the non-local interactions in such small band-gap systems. After increasing the impurity size, we find that DMFT gives better agreement with the reference EOM-CCSD spectrum. The DMFT(i104,b128) calculation finds the $\Gamma \rightarrow \mathbf{X}$ gap to be 1.78 eV, reducing the DMFT(i26,b32) error to 0.5 eV. This is also better than the $2 \times 2 \times 1$ \mathbf{k} -point EOM-CCSD result, which estimates the $\Gamma \rightarrow \mathbf{X}$ gap to be 0.59 eV (~ 0.7 eV error). DMFT(i104,b128) does not produce a better band gap compared to DMFT(i26,b160) due to the insufficient bath size, suggesting that minimizing the bath discretization error is also important. Nevertheless, the DMFT(i104,b128) spectrum has an improved shape, especially in the valence region, where the bands have similar peak positions to the EOM-CCSD ones. Thus, bulk Si provides a good demonstration of the important role of impurity size in capturing the non-local self-energy in delocalized systems. However, even with the larger $2 \times 2 \times 1$ impurity, the DMFT results are still not completely accurate, indicating the need for both larger impurities and a better treatment of long-range

interactions than the HF self-energy.

4.3 NiO

We finally turn to discuss the prototypical strongly-correlated system, NiO. NiO has a type-II AFM phase below the Néel temperature (525 K), with ferromagnetic planes stacked in the [111] direction. Due to the partially filled d orbitals in Ni, spin-unpolarized DFT methods predict NiO to be a metal, and spin-polarized DFT (LSDA/GGA) significantly underestimates the band gap and magnetic moment. DFT+DMFT simulations with a single Ni $3d$ impurity have been shown to successfully reproduce features of the experimental spectral functions and band structure of NiO in the paramagnetic (PM) phase.^{34,88–93}

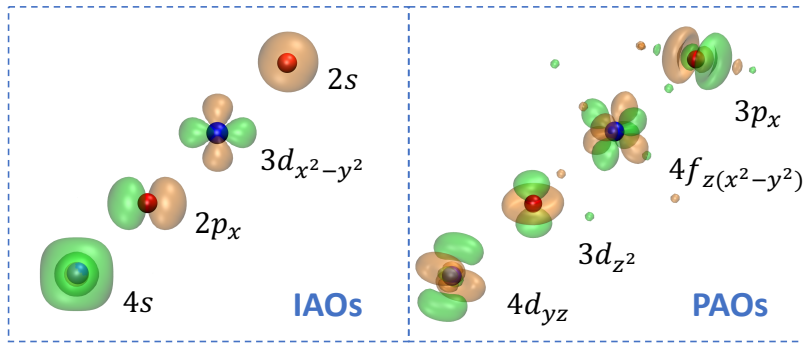


Figure 4: Representative IAOs and PAOs of NiO used in DMFT calculations within a unit cell. Ni and O atoms are marked in blue and red.

In this study, we use a unit cell of two Ni and two O atoms as the impurity in DMFT, corresponding to 78 impurity orbitals. Compared to earlier single site studies, we can thus examine antiferromagnetic order within the cell, as well as the effect of all the interactions in the crystal bands. Some representative IAOs and PAOs in the cell are shown in Fig. 4. The IAOs include the projected $3s3p3d4s$ orbitals of Ni and $2s2p$ orbitals of O, and the PAOs include the remaining $4p4d4f5s$ orbitals of Ni and $3s3p3d$ orbitals of O. Since the $3s3p$ orbitals of Ni form very flat bands far below the Fermi surface, we do not couple bath orbitals to them, to reduce the computational cost. We also used the bath truncation

technique described in Sec. 2.2 to remove very weakly coupled bath orbitals, setting the eigenvalue threshold to $\lambda = 0.005$ a.u. and $\lambda = 0.01$ a.u. for Gauss-Legendre quadratures of $N_\omega = 4$ and $N_\omega = 8$ respectively. This led to a significant reduction in the number of bath orbitals, e.g., from $N_b = 160$ to $N_b = 86$ in the DMFT(i78,b86)@ Φ_{UHF} calculation.

To obtain an AFM solution in DMFT, we allowed spin symmetry to break by allowing different self-energies ($\Sigma_{\text{imp}}^\sigma(\omega)$) and hybridizations ($\Delta^\sigma(\omega)$) in different spin channels ($\sigma = \alpha, \beta$). The spin-unrestricted CCSD-GF (UCCSD-GF) impurity solver was employed to compute $\Sigma_{\text{imp}}^\sigma(\omega)$. We started from either spin-restricted or spin-unrestricted mean-field wavefunctions to construct the embedding problem. Spin-unrestricted HF (UHF) gives an AFM solution with a large band gap for NiO, as shown in Fig. 5. Starting from UHF, spin symmetry breaking happens already in the initial DMFT impurity Hamiltonian (\mathbf{H}_{imp}) and lattice HF self-energy. On the other hand, spin-restricted HF (RHF) with finite temperature smearing predicts NiO to be a metal (in PM phase), with no average local magnetic moment (Fig. 5). In this case, spin symmetry breaking is introduced *only* during DMFT self-consistency, which generates symmetry-broken $\Sigma_{\text{imp}}^\sigma(\omega)$ and $\Delta^\sigma(\omega)$.

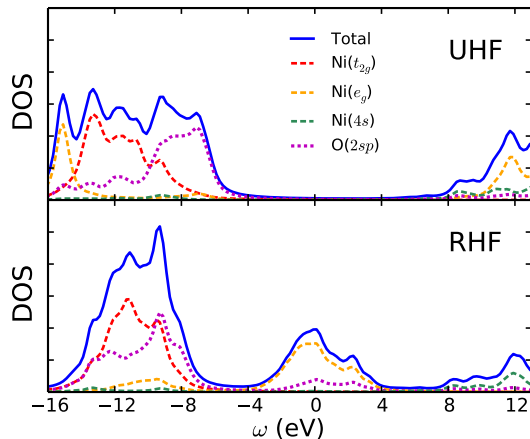


Figure 5: Local density of states of NiO from UHF and RHF. A broadening factor $\eta = 0.4$ eV is used.

In addition to starting from HF orbitals, we also explored the possibility of using DFT (LDA and PBE) orbitals to generate the DMFT impurity problem. We again emphasize that

only the DFT orbitals were used here and no DFT Hamiltonians or self-energies enter into our DMFT calculations. That is to say, we still use the Fock matrix as the one-particle effective Hamiltonian, and the only difference is that the elements of the Fock matrix are evaluated using DFT orbitals. Since the local Fock self-energy can be exactly subtracted, there are no double counting errors in these DMFT calculations. One advantage of using DFT orbitals is that fully self-consistent HF calculations can be avoided, which is very expensive in large systems due to the quadratic scaling with respect to \mathbf{k} points.

Table 2: Band gap (E_g), magnetic moment (m_{Ni}) and local charge (ρ_{Ni}) of NiO in the AFM phase. The first column of band gaps is computed from the half maxima of the first valence and conduction bands of the local DOS, as done in Ref.⁹⁴ The second column of band gaps (in brackets) is computed from the valence and conduction peaks of the \mathbf{k} -resolved DOS. The notation “@ $\Phi_{\text{HF/PBE/LDA}}$ ” indicates the underlying orbitals used to construct the Fock matrix in DMFT.

Method	E_g (eV)	m_{Ni} (μ_{B})	ρ_{Ni} (e)
UHF	- (11.6)	1.86	1.42
UPBE	- (1.3)	1.42	1.02
ULDA	- (0.6)	1.28	0.94
DMFT(i78,b50)@ Φ_{UHF}	9.6 (9.4)	1.80	1.35
DMFT(i78,b86)@ Φ_{UHF}	9.2 (9.0)	1.80	1.35
DMFT(i78,b52)@ Φ_{UPBE}	7.4 (7.1)	1.65	1.12
DMFT(i78,b90)@ Φ_{UPBE}	7.1 (6.5)	1.63	1.11
DMFT(i78,b52)@ Φ_{ULDA}	6.5 (6.0)	1.63	1.10
DMFT(i78,b90)@ Φ_{ULDA}	6.5 (5.8)	1.60	1.08
DMFT(i78,b56)@ Φ_{RHF}	3.5 (3.3)	1.67	1.22
DMFT(i78,b98)@ Φ_{RHF}	3.0 (3.1)	1.60	1.17
Exp	4.3 ⁹⁴ (-)	1.77, ⁹⁵ 1.90 ⁸⁰	-

We present DMFT results on the band gap, magnetic moments and local charges of NiO in Table 2. The band gap is computed from the half maxima of the first valence and conduction bands of local DOS, as done in the XPS/BIS experiment.⁹⁴ Meanwhile, we also report the band gap values calculated from the valence and conduction peaks of the \mathbf{k} -resolved DOS. The magnetic moments and local charges are calculated from the impurity UCCSD density matrix with atomic decomposition in the IAO+PAO basis. As can be seen, DMFT(i78,b86)@ Φ_{UHF} improves the UHF band gap by 2.6 eV and produces an accurate

magnetic moment. However, the band gap is still too large when compared to experiment (4.3 eV). This is likely because the off-diagonal (inter-cell) part of the self-energy from the inaccurate initial UHF solution has a large residual effect on the lattice Green’s function. In particular, this inaccurate off-diagonal self-energy leads to too large an amount of symmetry breaking in the initial impurity Hamiltonian, which cannot be completely corrected by the DMFT local self-energy. In contrast, when using UPBE orbitals, DMFT(i78,b90)@ Φ_{UPBE} gives a better \mathbf{k} -resolved band gap of 6.5 eV, suggesting that employing UPBE orbitals reduces the error in the off-diagonal HF self-energy. Using ULDA orbitals further improves the \mathbf{k} -resolved band gap to 5.8 eV, although the error is still more than 1 eV. Overall, these results show that when starting from a spin-symmetry broken solution, our DMFT scheme is sensitive to the choice of underlying orbitals, which may lead to a variation of 3 eV in the predicted band gap of NiO. This sensitivity may be alleviated if charge self-consistency is further imposed outside of the DMFT loop,^{96,97} which is absent in our current implementation. However, the systematic overestimation of the band gap suggests that besides charge self-consistency, non-local contributions to the self-energy need to be treated more accurately.^{49,50,98,99}

When we switch to a spin-restricted HF reference, the DMFT results are more accurate than the UHF-based DMFT results. DMFT(i78,b98)@ Φ_{RHF} predicts a reasonable \mathbf{k} -resolved band gap of 3.1 eV and magnetic moment of 1.60 μ_{B} . This superior performance can be attributed to the fact that the initial incorrect symmetry breaking in the lattice HF self-energy and impurity Hamiltonian is avoided by using a spin-restricted reference. As a result, the spin symmetry breaking is solely determined by the accurate DMFT self-energy obtained from the UCCSD-GF impurity solver, leading to improved results, particularly for the spectral functions.

We present the local DOS of NiO in Fig. 6. The upper panel shows that DMFT(i78,b86)@ Φ_{ULDA} gives a similar spectral shape to experiment, although the band gap is larger and the first valence peak is broader. On the other hand, DMFT(i78,b90)@ Φ_{UHF} spectrum has too wide

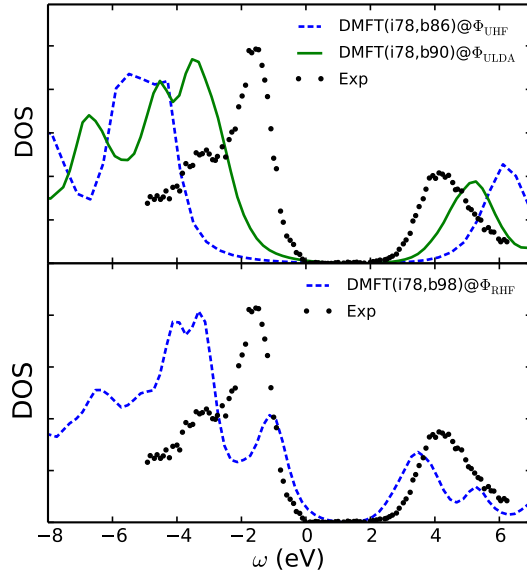


Figure 6: Local density of states of NiO in the AFM phase. The XPS/BIS experimental DOS is from Ref. ⁹⁴ The DMFT DOS is computed with a broadening factor $\eta = 0.4$ eV, and is shifted horizontally for an easier comparison to experiment.

a band gap. In the lower panel, the DMFT(i78,b98) Φ_{RHF} result agrees well with experiment near the Fermi surface. However, the main valence peak is separated into two peaks, where the highest peak is around -3.5 eV and a shoulder peak appears around -1 eV. Such a two-peak structure is not observed in experiment.

To understand the deviations from experiment and to further study the character of the insulating gap, we plot the components of the NiO DOS in Fig. 7. From Panel 1 of Fig. 7(a), DMFT(i78,b90) Φ_{ULDA} predicts that the insulating gap is from a complicated charge transfer transition with mixed Mott character: the valence peak is of O $2sp$ and Ni t_{2g} and e_g characters, and the conduction peak is mainly of an e_g character with a small O $2sp$ contribution. On the other hand, it can be seen in Fig. 5 that UHF predicts the insulating gap of NiO to be from a pure charge transfer transition from O $2p$ to Ni e_g . This comparison indicates that DMFT significantly corrects the positions of the Ni t_{2g} and e_g bands. Meanwhile, as shown in Fig. 7(b), DMFT(i78,b98) Φ_{RHF} also predicts mixed charge transfer and Mott character for the insulating gap, although the first valence peak

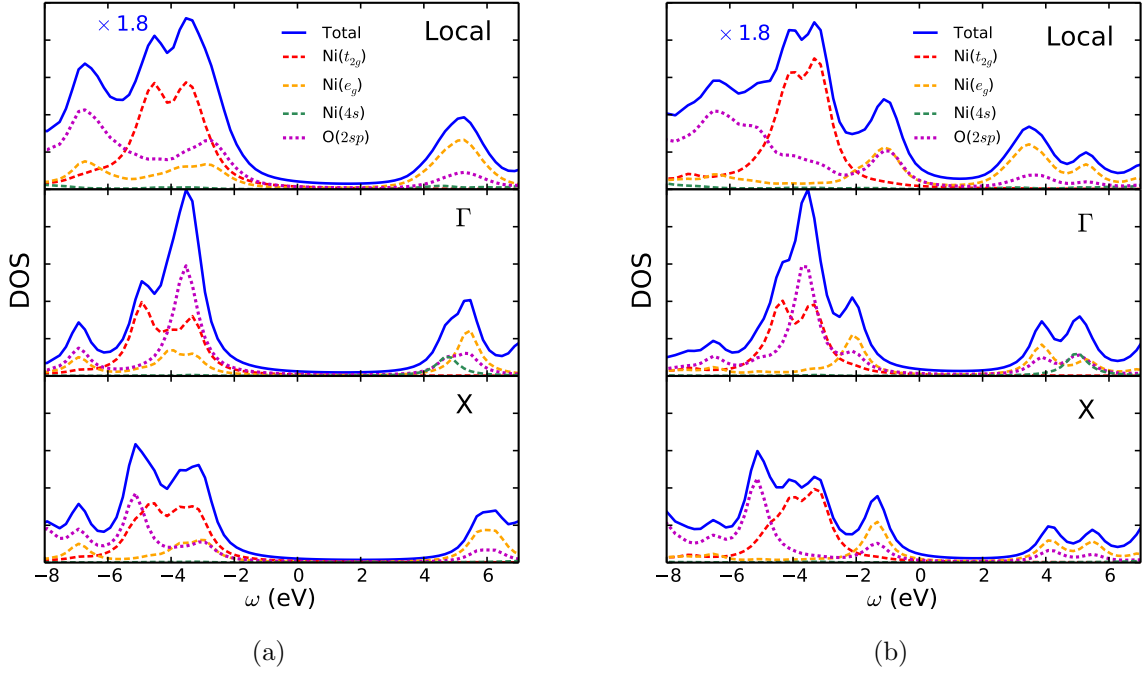


Figure 7: Components of NiO density of states from (a) DMFT(i78,b90) $@\Phi_{\text{ULDA}}$ and (b) DMFT(i78,b98) $@\Phi_{\text{RHF}}$ calculations. Panel 1 shows the local DOS, and Panels 2 and 3 show \mathbf{k} -resolved DOS at Γ and \mathbf{X} points.

has almost no Ni t_{2g} contribution. This indicates that the artificial shoulder valence peak near the Fermi surface arises because of a mismatch in the relative positions of the Ni t_{2g} and O $2sp$ /Ni e_g bands. Once again, these results lead us to conclude that to obtain both the band gap and spectral shape accurately, we require either larger impurities or a more sophisticated treatment of the inter-cluster interactions. We also plot the \mathbf{k} -resolved DOS in Panels 2 and 3 in Fig. 7. It can be seen that the O $2sp$ main valence peak is shifted by 2 eV at the \mathbf{X} point compared to the Γ point. Interestingly, we find that the conduction band at the Γ point has a significant contribution from the Ni $4s$ and O $2sp$ orbitals. This has not been reported in previous DFT+DMFT studies but has also been found in quasiparticle self-consistent GW calculations¹⁰⁰ and a recent periodic EOM-CCSD calculation.¹⁰¹

5 Conclusions

In this work, we described a new *ab initio* DMFT scheme for studying realistic solid-state materials using both large impurities, spanning multiple unit cells and atoms, and realistic quantum chemical basis sets. The use of Hartree-Fock as the low-level method allowed us to avoid empirical parametrizations and double counting errors. By employing the computational infrastructure of the intrinsic atomic orbital/projected atomic orbital basis, fast integral transformations, and bath truncation, we showed that we could efficiently construct the DMFT embedding Hamiltonian. Finally, combining this scheme with coupled-cluster impurity solvers enabled us to solve the impurity problem with several hundred embedding orbitals. Our numerical results on 2D h-BN, bulk Si and NiO (in the antiferromagnetic phase) were encouraging and demonstrated the promise of *ab initio* DMFT in the simulation of both weakly and strongly correlated materials. Future work will explore the impact of charge self-consistency and a more accurate treatment of long-range interactions.

Acknowledgement

We thank Timothy Berkelbach and Yang Gao for helpful discussions. This work is supported by the US DOE via de-sc0018140. Additional support was provided by the Simons Foundation via the Simons Collaboration on the Many-Electron Problem, and via the Simons Investigatorship in Physics.

Supporting Information Available

The following files are available free of charge. Comparison of IAO-only and IAO+PAO hybridizations and causality of the CCSD self-energy in DMFT.

References

- (1) Georges, A.; Kotliar, G. Hubbard model in infinite dimensions. *Phys. Rev. B* **1992**, *45*, 6479.
- (2) Georges, A.; Kotliar, G.; Krauth, W.; Rozenberg, M. Dynamical mean-field theory of strongly correlated fermion systems and the limit of infinite dimensions. *Rev. Mod. Phys.* **1996**, *68*, 13.
- (3) Lichtenstein, A. I.; Katsnelson, M. I. Antiferromagnetism and d-wave superconductivity in cuprates: A cluster dynamical mean-field theory. *Phys. Rev. B* **2000**, *62*, R9283–R9286.
- (4) Kotliar, G.; Savrasov, S. Y.; Pálsson, G.; Biroli, G. Cellular dynamical mean field approach to strongly correlated systems. *Phys. Rev. Lett.* **2001**, *87*, 186401–1–186401–4.
- (5) Hettler, M.; Mukherjee, M.; Jarrell, M.; Krishnamurthy, H. Dynamical cluster approximation: Nonlocal dynamics of correlated electron systems. *Phys. Rev. B* **2000**, *61*, 12739.
- (6) Maier, T.; Jarrell, M.; Pruschke, T.; Hettler, M. H. Quantum cluster theories. *Rev. Mod. Phys.* **2005**, *77*, 1027.
- (7) Metzner, W.; Vollhardt, D. Correlated lattice fermions in $d = \infty$ dimensions. *Phys. Rev. Lett.* **1989**, *62*, 324–327.
- (8) Zgid, D.; Chan, G. K.-L. Dynamical mean-field theory from a quantum chemical perspective. *J. Chem. Phys.* **2011**, *134*, 094115.
- (9) Kohn, W.; Sham, L. J. Self-consistent equations including exchange and correlation effects. *Phys. Rev.* **1965**, *140*, A1133–A1138.

- (10) Kotliar, G.; Savrasov, S. Y.; Haule, K.; Oudovenko, V. S.; Parcollet, O.; Marianetti, C. A. Electronic structure calculations with dynamical mean-field theory. *Rev. Mod. Phys.* **2006**, *78*, 865–951.
- (11) Held, K.; Nekrasov, I. A.; Keller, G.; Eyert, V.; Blümer, N.; McMahan, A. K.; Scalettar, R. T.; Pruschke, T.; Anisimov, V. I.; Vollhardt, D. Realistic investigations of correlated electron systems with LDA + DMFT. *Phys. status solidi* **2006**, *243*, 2599–2631.
- (12) Held, K. Electronic structure calculations using dynamical mean field theory. *Adv. Phys.* **2007**, *56*, 829–926.
- (13) Andersen, O. K.; Saha-Dasgupta, T. Muffin-tin orbitals of arbitrary order. *Phys. Rev. B* **2000**, *62*, R16219–R16222.
- (14) Werner, P.; Millis, A. J. Dynamical screening in correlated electron materials. *Phys. Rev. Lett.* **2010**, *104*, 146401.
- (15) Werner, P.; Casula, M. Dynamical screening in correlated electron systems - from lattice models to realistic materials. *J. Phys. Condens. Matter* **2016**, *28*, 383001.
- (16) Anisimov, V. I.; Zaanen, J.; Andersen, O. K. Band theory and Mott insulators: Hubbard U instead of Stoner I. *Phys. Rev. B* **1991**, *44*, 943–954.
- (17) Kanamori, J. Electron correlation and ferromagnetism of transition metals. *Prog. Theor. Phys.* **1963**, *30*, 275–289.
- (18) Hybertsen, M. S.; Stechel, E. B.; Schluter, M.; Jennison, D. R. Renormalization from density-functional theory to strong-coupling models for electronic states in Cu-O materials. *Phys. Rev. B* **1990**, *41*, 11068–11072.
- (19) Lichtenstein, A. I.; Katsnelson, M. I.; Kotliar, G. Finite-temperature magnetism of

- transition metals: An ab initio dynamical mean-field theory. *Phys. Rev. Lett.* **2001**, *87*, 067205.
- (20) Aryasetiawan, F.; Imada, M.; Georges, A.; Kotliar, G.; Biermann, S.; Lichtenstein, A. I. Frequency-dependent local interactions and low-energy effective models from electronic structure calculations. *Phys. Rev. B* **2004**, *70*, 195104.
- (21) Aryasetiawan, F.; Karlsson, K.; Jepsen, O.; Schönberger, U. Calculations of Hubbard U from first-principles. *Phys. Rev. B* **2006**, *74*, 125106.
- (22) Vaugier, L.; Jiang, H.; Biermann, S. Hubbard U and Hund exchange J in transition metal oxides: Screening versus localization trends from constrained random phase approximation. *Phys. Rev. B* **2012**, *86*, 165105.
- (23) Werner, P.; Comanac, A.; de' Medici, L.; Troyer, M.; Millis, A. J. Continuous-time solver for quantum impurity models. *Phys. Rev. Lett.* **2006**, *97*, 076405.
- (24) Gull, E.; Werner, P.; Parcollet, O.; Troyer, M. Continuous-time auxiliary-field Monte Carlo for quantum impurity models. *EPL (Europhys. Lett.)* **2008**, *82*, 57003.
- (25) Gull, E.; Millis, A. J.; Lichtenstein, A. I.; Rubtsov, A. N.; Troyer, M.; Werner, P. Continuous-time Monte Carlo methods for quantum impurity models. *Rev. Mod. Phys.* **2011**, *83*, 349–404.
- (26) Caffarel, M.; Krauth, W. Exact diagonalization approach to correlated fermions in infinite dimensions: Mott transition and superconductivity. *Phys. Rev. Lett.* **1994**, *72*, 1545–1548.
- (27) Capone, M.; de' Medici, L.; Georges, A. Solving the dynamical mean-field theory at very low temperatures using the Lanczos exact diagonalization. *Phys. Rev. B* **2007**, *76*, 245116.

- (28) Zgid, D.; Gull, E.; Chan, G. K. L. Truncated configuration interaction expansions as solvers for correlated quantum impurity models and dynamical mean-field theory. *Phys. Rev. B* **2012**, *86*, 1–12.
- (29) Bulla, R.; Costi, T. A.; Pruschke, T. Numerical renormalization group method for quantum impurity systems. *Rev. Mod. Phys.* **2008**, *80*, 395–450.
- (30) White, S. R. Density matrix formulation for quantum renormalization groups. *Phys. Rev. Lett.* **1992**, *69*, 2863–2866.
- (31) Gutzwiller, M. C. Effect of correlation on the ferromagnetism of transition metals. *Phys. Rev. Lett.* **1963**, *10*, 159–162.
- (32) Kuramoto, Y. Self-consistent perturbation theory for dynamics of valence fluctuations. *Z Phys. B* **1983**, *53*, 37–52.
- (33) Zhu, T.; Jiménez-Hoyos, C. A.; McClain, J.; Berkelbach, T. C.; Chan, G. K.-L. Coupled-cluster impurity solvers for dynamical mean-field theory. *Phys. Rev. B* **2019**, *100*, 115154.
- (34) Karolak, M.; Ulm, G.; Wehling, T.; Mazurenko, V.; Poteryaev, A.; Lichtenstein, A. Double counting in LDA+DMFT - The example of NiO. *J. Electron Spectros. Relat. Phenom.* **2010**, *181*, 11–15.
- (35) Wang, X.; Han, M. J.; de' Medici, L.; Park, H.; Marianetti, C. A.; Millis, A. J. Covalency, double-counting, and the metal-insulator phase diagram in transition metal oxides. *Phys. Rev. B* **2012**, *86*, 195136.
- (36) Haule, K. Exact double counting in combining the dynamical mean field theory and the density functional theory. *Phys. Rev. Lett.* **2015**, *115*, 196403.
- (37) Pollet, R.; Savin, A.; Leininger, T.; Stoll, H. Combining multideterminantal wave

- functions with density functionals to handle near-degeneracy in atoms and molecules. *J. Chem. Phys.* **2002**, *116*, 1250–1258.
- (38) Gagliardi, L.; Truhlar, D. G.; Li Manni, G.; Carlson, R. K.; Hoyer, C. E.; Bao, J. L. Multiconfiguration pair-density functional theory: A new way to treat strongly correlated systems. *Acc. Chem. Res.* **2017**, *50*, 66–73.
- (39) Zhu, T.; de Silva, P.; van Aggelen, H.; Van Voorhis, T. Many-electron expansion: A density functional hierarchy for strongly correlated systems. *Phys. Rev. B* **2016**, *93*, 201108.
- (40) Zhu, T.; de Silva, P.; Van Voorhis, T. Implementation of the many-pair expansion for systematically improving density functional calculations of molecules. *J. Chem. Theory Comput.* **2019**, *15*, 1089–1101.
- (41) Shinaoka, H.; Troyer, M.; Werner, P. Accuracy of downfolding based on the constrained random-phase approximation. *Phys. Rev. B* **2015**, *91*, 245156.
- (42) Honerkamp, C.; Shinaoka, H.; Assaad, F. F.; Werner, P. Limitations of constrained random phase approximation downfolding. *Phys. Rev. B* **2018**, *98*, 235151.
- (43) Wang, X.; Gull, E.; de’ Medici, L.; Capone, M.; Millis, A. J. Antiferromagnetism and the gap of a Mott insulator: Results from analytic continuation of the self-energy. *Phys. Rev. B* **2009**, *80*, 045101.
- (44) Liebsch, A.; Ishida, H. Temperature and bath size in exact diagonalization dynamical mean field theory. *J. Phys. Condens. Matter* **2012**, *24*, 053201.
- (45) Lin, C.; Demkov, A. A. Efficient variational approach to the impurity problem and its application to the dynamical mean-field theory. *Phys. Rev. B* **2013**, *88*, 035123.
- (46) Lu, Y.; Höppner, M.; Gunnarsson, O.; Haverkort, M. Efficient real-frequency solver for dynamical mean-field theory. *Phys. Rev. B* **2014**, *90*, 085102.

- (47) Go, A.; Millis, A. J. Adaptively truncated Hilbert space based impurity solver for dynamical mean-field theory. *Phys. Rev. B* **2017**, *96*, 1–11.
- (48) Lin, N.; Marianetti, C. A.; Millis, A. J.; Reichman, D. R. Dynamical mean-field theory for quantum chemistry. *Phys. Rev. Lett.* **2011**, *106*, 096402.
- (49) Sun, P.; Kotliar, G. Extended dynamical mean-field theory and **GW** method. *Phys. Rev. B* **2002**, *66*, 085120.
- (50) Biermann, S.; Aryasetiawan, F.; Georges, A. First-principles approach to the electronic structure of strongly correlated systems: combining the *GW* approximation and dynamical mean-field theory. *Phys. Rev. Lett.* **2003**, *90*, 086402.
- (51) Boehnke, L.; Nilsson, F.; Aryasetiawan, F.; Werner, P. When strong correlations become weak: Consistent merging of *GW* and DMFT. *Phys. Rev. B* **2016**, *94*, 201106.
- (52) Kananenka, A. A.; Gull, E.; Zgid, D. Systematically improvable multiscale solver for correlated electron systems. *Phys. Rev. B* **2015**, *91*, 121111.
- (53) Lan, T. N.; Kananenka, A. A.; Zgid, D. Communication: Towards ab initio self-energy embedding theory in quantum chemistry. *J. Chem. Phys.* **2015**, *143*, 241102.
- (54) Rusakov, A. A.; Iskakov, S.; Tran, L. N.; Zgid, D. Self-energy embedding theory (SEET) for periodic systems. *J. Chem. Theory Comput.* **2019**, *15*, 229–240.
- (55) Choi, S.; Kutepov, A.; Haule, K.; van Schilfhaarde, M.; Kotliar, G. First-principles treatment of Mott insulators: linearized QSGW+DMFT approach. *npj Quantum Mater.* **2016**, *1*, 16001.
- (56) Sun, Q.; Berkelbach, T. C.; Blunt, N. S.; Booth, G. H.; Guo, S.; Li, Z.; Liu, J.; McClain, J. D.; Sayfutyarova, E. R.; Sharma, S.; Wouters, S.; Chan, G. K.-L. PySCF: the Python-based simulations of chemistry framework. *Wiley Interdiscip. Rev. Comput. Mol. Sci.* **2018**, *8*, e1340.

- (57) TURBOMOLE V7.4 2019, a development of University of Karlsruhe and Forschungszentrum Karlsruhe GmbH, 1989-2007, TURBOMOLE GmbH, since 2007; available from <http://www.turbomole.com>.
- (58) Ronca, E.; Li, Z.; Jimenez-Hoyos, C. A.; Chan, G. K.-L. Time-step targeting time-dependent and dynamical density matrix renormalization group algorithms with ab initio Hamiltonians. *J. Chem. Theory Comput.* **2017**, *13*, 5560–5571.
- (59) McClain, J.; Lischner, J.; Watson, T.; Matthews, D. A.; Ronca, E.; Louie, S. G.; Berkelbach, T. C.; Chan, G. K.-L. Spectral functions of the uniform electron gas via coupled-cluster theory and comparison to the GW and related approximations. *Phys. Rev. B* **2016**, *93*, 235139.
- (60) Shee, A.; Zgid, D. Coupled cluster as an impurity solver for Green’s Function embedding methods. *J. Chem. Theory Comput.* **2019**, *15*, 6010–6024.
- (61) Knizia, G.; Chan, G. K.-L. Density matrix embedding: A simple alternative to dynamical mean-field theory. *Phys. Rev. Lett.* **2012**, *109*, 186404.
- (62) Knizia, G.; Chan, G. K.-L. Density matrix embedding: A strong-coupling quantum embedding theory. *J. Chem. Theory Comput.* **2013**, *9*, 1428–1432.
- (63) Wouters, S.; Jiménez-Hoyos, C. A.; Sun, Q.; Chan, G. K.-L. A practical guide to density matrix embedding theory in quantum chemistry. *J. Chem. Theory Comput.* **2016**, *12*, 2706–2719.
- (64) Cui, Z.-H.; Zhu, T.; Chan, G. K.-L. Efficient implementation of ab initio quantum embedding in periodic systems: density matrix embedding theory. *arXiv:1909.08596* **2019**,
- (65) Pulay, P. Convergence acceleration of iterative sequences. the case of scf iteration. *Chem. Phys. Lett.* **1980**, *73*, 393–398.

- (66) Knizia, G. Intrinsic atomic orbitals: An unbiased bridge between quantum theory and chemical concepts. *J. Chem. Theory Comput.* **2013**, *9*, 4834–4843.
- (67) Whitten, J. L. Coulombic potential energy integrals and approximations. *J. Chem. Phys.* **1973**, *58*, 4496–4501.
- (68) Sun, Q.; Berkelbach, T. C.; McClain, J. D.; Chan, G. K.-L. Gaussian and plane-wave mixed density fitting for periodic systems. *J. Chem. Phys.* **2017**, *147*, 164119.
- (69) Peters, R. Spectral functions for single- and multi-impurity models using density matrix renormalization group. *Phys. Rev. B* **2011**, *84*, 075139.
- (70) Ganahl, M.; Aichhorn, M.; Evertz, H. G.; Thunström, P.; Held, K.; Verstraete, F. Efficient DMFT impurity solver using real-time dynamics with matrix product states. *Phys. Rev. B* **2015**, *92*, 155132.
- (71) Koch, E.; Sangiovanni, G.; Gunnarsson, O. Sum rules and bath parametrization for quantum cluster theories. *Phys. Rev. B* **2008**, *78*, 115102.
- (72) Wolf, F. A.; Go, A.; McCulloch, I. P.; Millis, A. J.; Schollwöck, U. Imaginary-time matrix product state impurity solver for dynamical mean-field theory. *Phys. Rev. X* **2015**, *5*, 041032.
- (73) de Vega, I.; Schollwöck, U.; Wolf, F. A. How to discretize a quantum bath for real-time evolution. *Phys. Rev. B* **2015**, *92*, 155126.
- (74) Nooijen, M.; Snijders, J. G. Coupled cluster approach to the single-particle Green’s function. *Int. J. Quantum Chem.* **1992**, *44*, 55–83.
- (75) Nooijen, M.; Snijders, J. G. Coupled cluster Green’s function method: Working equations and applications. *Int. J. Quantum Chem.* **1993**, *48*, 15–48.
- (76) Bhaskaran-Nair, K.; Kowalski, K.; Shelton, W. A. Coupled cluster Green function: Model involving single and double excitations. *J. Chem. Phys.* **2016**, *144*, 144101.

- (77) Furukawa, Y.; Kosugi, T.; Nishi, H.; Matsushita, Y.-i. Band structures in coupled-cluster singles-and-doubles Green's function (GFCCSD). *J. Chem. Phys.* **2018**, *148*, 204109.
- (78) Li, L. H.; Chen, Y.; Behan, G.; Zhang, H.; Petracic, M.; Glushenkov, A. M. Large-scale mechanical peeling of boron nitride nanosheets by low-energy ball milling. *J. Mater. Chem.* **2011**, *21*, 11862.
- (79) Töbrens, D.; Stüßer, N.; Knorr, K.; Mayer, H.; Lampert, G. E9: The new high-resolution neutron powder diffractometer at the Berlin Neutron Scattering Center. European Powder Diffraction EPDIC 7. 2001; pp 288–293.
- (80) Cheetham, A. K.; Hope, D. A. O. Magnetic ordering and exchange effects in the antiferromagnetic solid solutions $\text{Mn}_x\text{Ni}_{1-x}\text{O}$. *Phys. Rev. B* **1983**, *27*, 6964.
- (81) Goedecker, S.; Teter, M.; Hutter, J. Separable dual-space Gaussian pseudopotentials. *Phys. Rev. B* **1996**, *54*, 1703.
- (82) Hartwigsen, C.; Goedecker, S.; Hutter, J. Relativistic separable dual-space Gaussian pseudopotentials from H to Rn. *Phys. Rev. B* **1998**, *58*, 3641.
- (83) VandeVondele, J.; Hutter, J. Gaussian basis sets for accurate calculations on molecular systems in gas and condensed phases. *J. Chem. Phys.* **2007**, *127*, 114105.
- (84) de Sturler, E. Truncation strategies for optimal Krylov subspace methods. *SIAM J. Numer. Anal.* **1999**, *36*, 864–889.
- (85) Perdew, J. P.; Burke, K.; Ernzerhof, M. Generalized gradient approximation made simple. *Phys. Rev. Lett.* **1996**, *77*, 3865.
- (86) Stanton, J. F.; Bartlett, R. J. The equation of motion coupled-cluster method. A systematic biorthogonal approach to molecular excitation energies, transition probabilities, and excited state properties. *J. Chem. Phys.* **1993**, *98*, 7029–7039.

- (87) McClain, J.; Sun, Q.; Chan, G. K.-L.; Berkelbach, T. C. Gaussian-based coupled-cluster theory for the ground-state and band structure of solids. *J. Chem. Theory Comput.* **2017**, *13*, 1209–1218.
- (88) Ren, X.; Leonov, I.; Keller, G.; Kollar, M.; Nekrasov, I.; Vollhardt, D. LDA + DMFT computation of the electronic spectrum of NiO. *Phys. Rev. B* **2006**, *74*, 195114.
- (89) Kuneš, J.; Anisimov, V. I.; Skornyakov, S. L.; Lukoyanov, A. V.; Vollhardt, D. NiO: Correlated band structure of a charge-transfer insulator. *Phys. Rev. Lett.* **2007**, *99*, 156404.
- (90) Kuneš, J.; Anisimov, V. I.; Lukoyanov, A. V.; Vollhardt, D. Local correlations and hole doping in NiO: A dynamical mean-field study. *Phys. Rev. B* **2007**, *75*, 165115.
- (91) Yin, Q.; Gordienko, A.; Wan, X.; Savrasov, S. Y. Calculated momentum dependence of Zhang-Rice states in transition metal oxides. *Phys. Rev. Lett.* **2008**, *100*, 066406.
- (92) Thunström, P.; Di Marco, I.; Eriksson, O. Electronic entanglement in late transition metal oxides. *Phys. Rev. Lett.* **2012**, *109*, 186401.
- (93) Leonov, I.; Pourovskii, L.; Georges, A.; Abrikosov, I. A. Magnetic collapse and the behavior of transition metal oxides at high pressure. *Phys. Rev. B* **2016**, *94*, 155135.
- (94) Sawatzky, G. A.; Allen, J. W. Magnitude and origin of the band gap in NiO. *Phys. Rev. Lett.* **1984**, *53*, 2339–2342.
- (95) Fender, B. E. F.; Jacobson, A. J.; Wedgwood, F. A. Covalency parameters in MnO, α MnS, and NiO. *J. Chem. Phys.* **1968**, *48*, 990–994.
- (96) Grånäs, O.; Di Marco, I.; Thunström, P.; Nordström, L.; Eriksson, O.; Björkman, T.; Wills, J. Charge self-consistent dynamical mean-field theory based on the full-potential linear muffin-tin orbital method: Methodology and applications. *Comput. Mater. Sci.* **2012**, *55*, 295–302.

- (97) Park, H.; Millis, A. J.; Marianetti, C. A. Computing total energies in complex materials using charge self-consistent DFT+DMFT. *Phys. Rev. B* **2014**, *90*, 235103.
- (98) Si, Q.; Smith, J. L. Kosterlitz-thouless transition and short range spatial correlations in an extended hubbard model. *Phys. Rev. Lett.* **1996**, *77*, 3391–3394.
- (99) Sun, P.; Kotliar, G. Many-body approximation scheme beyond GW. *Phys. Rev. Lett.* **2004**, *92*.
- (100) Das, S.; Coulter, J. E.; Manousakis, E. Convergence of quasiparticle self-consistent **GW** calculations of transition-metal monoxides. *Phys. Rev. B* **2015**, *91*, 115105.
- (101) Gao, Y.; Sun, Q.; Yu, J. M.; Motta, M.; McClain, J.; White, A. F.; Minnich, A. J.; Chan, G. K.-L. Electronic structure of bulk manganese oxide and nickel oxide from coupled cluster theory. *arXiv:1910.02191* **2019**,

Graphical TOC Entry

